0.1 E06-014

Precision Measurement of d_2^n: Probing the Lorentz Color Force

S. Choi, X. Jiang, Z.-E. Meziani, B. Sawatzky, spokespersons,
and
the d_2^n and Hall A Collaborations.
contributed by D. Parno, L. El Fassi, D. Flay, M. Posik, and Y. Zhang.

0.1.1 The Experiment

Experiment E06-014 ran in Hall A from February 7 to March 17, 2009, at production beam energies of 4.73 and 5.89 GeV, on a polarized ^{3}He target. The LHRS and BigBite were deployed as independent detectors, each oriented at an angle of 45° to the beamline. Each detector effectively operated as a single-arm experiment, with the LHRS measuring the unpolarized scattering cross section and BigBite measuring double-spin asymmetries in scattering between a longitudinally polarized electron beam and longitudinally and transversely polarized ^{3}He gas. The experiment was designed to provide extensive coverage of the deep inelastic scattering region, over ranges of $0.2 \leq x \leq 0.7$ and $2\ \text{GeV}^2 \leq Q^2 \leq 6\ \text{GeV}^2$.

This experiment ran immediately after E06-010, which used a similar configuration, and some calibration runs were shared between the two experiments. E06-014 was the commissioning experiment for a gas Čerenkov detector in the BigBite stack, as well as for a new photon detector and integrating data-acquisition system for the Compton polarimeter. Beamline calibrations have been completed, and detector calibrations are well underway.

Measurement of d_2^n The primary purpose of E06-014 is the measurement of the quantity d_2^n, a probe of the strong force that is formed by taking the second moment of a linear combination of the polarized structure functions g_1 and g_2, as follows:

$$d_2^n\left(Q^2\right) = \int_0^1 x^2 \left[2g_1^n\left(x, Q^2\right) + 3g_2^n\left(x, Q^2\right)\right] dx \tag{1}$$

In addition to the access it gives to quark-gluon correlations through its dependence on g_2^n, d_2^n is of physical interest in its own right. A precision measurement of this quantity can be used to test lattice QCD predictions. At low values of Q^2, d_2^n can be associated with spin polarizabilities within the nucleon [1, 2]. At high values of Q^2, d_2^n is best interpreted as a measure of the transverse color Lorentz force on a struck quark, averaged over the nucleon as a whole [1, 3].

E06-014 sought to accomplish the measurement of d_2^n in the deep inelastic scattering region by combining measurements of three quantities. With the LHRS, we took data for the measurement of the unpolarized total cross section σ_0. In BigBite, we took data for measuring two asymmetries formed between opposite target-beam spin configurations: $A_\parallel$, formed when both beam and target are polarized longitudinally, and $A_\perp$, formed when the target is polarized transverse to the longitudinal beam polarization. $A_\parallel$ and $A_\perp$ are typically measured as asymmetries in the counting rates for each spin configuration:

$$A_\parallel = \frac{N^{\downarrow\Uparrow} - N^{\uparrow\Uparrow}}{N^{\downarrow\Uparrow} + N^{\uparrow\Uparrow}} \quad \text{and} \quad A_\perp = \frac{N^{\downarrow\Rightarrow} - N^{\uparrow\Rightarrow}}{N^{\downarrow\Rightarrow} + N^{\uparrow\Rightarrow}}$$

Our independent measurements of σ_0, $A_\parallel$ and $A_\perp$ may then be combined into a measurement of d_2^n:

$$d_2^n = \int_0^1 \frac{MQ^2}{4\alpha^2} \frac{x^2y^2}{(1-y)(2-y)} \sigma_0 \left[\left(3\frac{1+(1-y)\cos\theta}{(1-y)\sin\theta} + \frac{4}{y}\tan\left(\theta/2\right)\right) A_\perp + \left(\frac{4}{y} - 3\right) A_\parallel\right] dx \tag{2}$$

where we have made use of the kinematic variables $x = Q^2/2M\nu$ (the Bjorken x variable), $\nu = E - E'$ (the energy transfer from electron to target), θ (the scattering angle of the electron), and $y = \nu/E$ (the fractional energy transfer from electron to target). This expression of d_2^n, in terms of directly measurable quantities rather than structure functions, allowed us to divide our allocated beam time so as to minimize the error on the d_2^n measurement itself, rather than the error on the measurements of g_1 and g_2. Our expectation is that

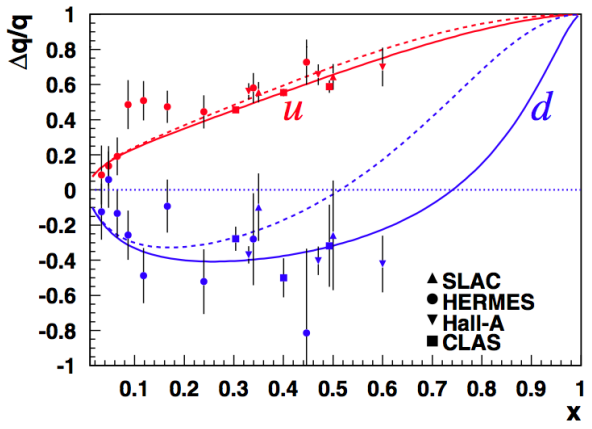

Figure 1: $\Delta q/q$ as a function of x, reproduced from Avakian *et al.* [11]. Dashed lines show the predictions of LSS(BBS) parameterizations, which use leading-order perturbative QCD with hadron helicity conservation [12]. Solid lines show predictions that explicitly include a nonzero term for the orbital angular momentum of valence quarks.

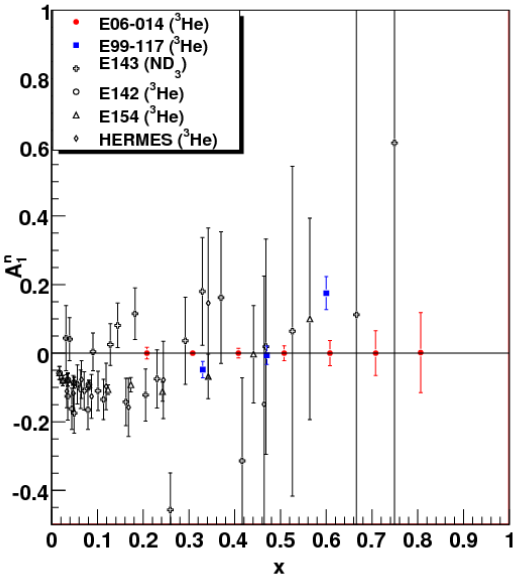

Figure 2: Projected statistical errors for E06-014's A_1^n measurement with 5.89 GeV beam are shown in red, along with results from previous experiments [7, 13, 14, 15, 16, 17]. The x bins are chosen to have a uniform width of 0.1.

the E06-014 measurement will represent a fourfold improvement in precision from previous world data [4], in advance of an approved 12 GeV experiment in Hall C that should push the precision and kinematic range still higher [5].

Measurement of A_1^n The data taken for the d_2^n measurement will also allow us to measure the longitudinal virtual photon-nucleon asymmetry for the neutron, A_1^n. When the nucleon and the virtual photon it exchanges with a lepton are both longitudinally polarized, the cross section of the process can be denoted $\sigma_{1/2(3/2)}$, where the subscript gives the projection of the total spin along the virtual photon's momentum direction when the spins are anti-parallel (parallel). A_1 is then defined as:

$$A_1\left(x,Q^2\right) \equiv \frac{\sigma_{1/2}-\sigma_{3/2}}{\sigma_{1/2}+\sigma_{3/2}} \approx \frac{g_1\left(x,Q^2\right)}{F_1\left(x,Q^2\right)} \text{ for high } Q^2 \tag{3}$$

We may also express A_1 in terms of the parallel and perpendicular asymmetries $A_\parallel$ and $A_\perp$:

$$A_1 = \frac{1}{D\left(1+\eta\xi\right)}A_\parallel - \frac{\eta}{d\left(1+\eta\xi\right)}A_\perp \tag{4}$$

where D is the virtual photon polarization factor and η, ξ, and d are quantities set by kinematics and by the virtual photon polarization vector.

Measuring A_1^n on an effective polarized neutron target (such as ^{3}He), when combined with measurements of A_1^p on a polarized proton target, gives access to the polarized-to-unpolarized parton distribution function

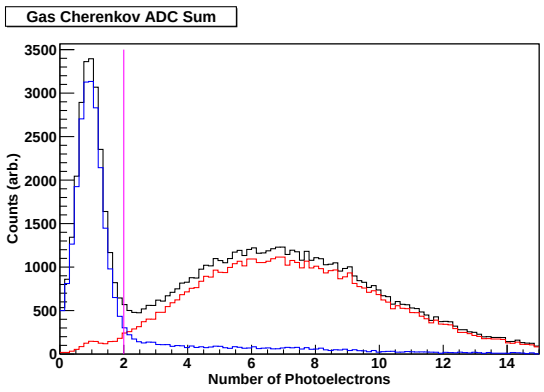

Figure 3: PID efficiency of LHRS gas Čerenkov. Pions are shown in blue and electrons in red, as determined by the pion rejectors. The magenta line shows the location of the proposed gas Čerenkov pion rejection cut, which gives a pion rejection factor of 600 while keeping 96% of electrons.

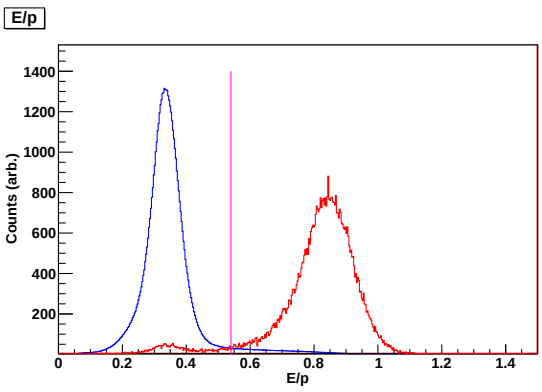

Figure 4: Pion and electron spectra in LHRS pion rejectors. The pion E/p spectrum is shown in blue and the electron spectrum in red, with these preliminary identifications determined by the gas Čerenkov; the spectra are normalized to have equal areas. The magenta line shows the location of the proposed pion rejector cut, which gives a pion rejection factor of 680 while keeping 99% of electrons.

ratios $\Delta u/u$ and $\Delta d/d$. Recent results from Hall A [6, 7] and from CLAS [8] showed a significant deviation of $\Delta d/d$ from the predictions of perturbative QCD, which have that ratio approaching 1 in the limit of $x \to 1$ (Figure 1). As part of the 12 GeV program, two approved experiments (one in Hall A [9] and one in Hall C [10]) will extend the accuracy and x range of this measurement, but a measurement of A_1^n at E06-014's kinematics will provide valuable support (or refutation) of prior Jefferson Lab results, while producing additional input for theoretical models in advance of the coming experiments at 12 GeV. Figure 2 shows existing world A_1^n data, as well as the projected statistical errors for the E06-014 measurement using a 5.9 GeV beam. (Projections for the $E_e = 4.7$ GeV dataset are not shown.)

0.1.2 Analysis Progress: Left HRS

Data from the Left HRS (LHRS) will be used to compute the total unpolarized cross section σ_0, which will contribute to our measurement of d_2^n. Here, we discuss our analysis progress on Left HRS data over the past year. In addition to the major points discussed below, we have confirmed that the E06-010 optics are suitable for the needs of this experiment, and have begun to study data quality over our six weeks of running.

Particle Identification Particle identification (PID) in the LHRS relies primarily on the gas Čerenkov and pion rejectors, whose efficiencies must be known to high precision in order to measure a cross section. Fortunately, the two detectors may be used to calibrate one another.

Figure 3 shows the gas Čerenkov ADC sum, in photoelectrons, at a typical kinematic setting. The blue histogram contains events labeled as pions by the pion rejector, while the red histogram contains events labeled as electrons. (The black spectrum is the sum of the two.) If a cut is placed at two photoelectrons (magenta line), 96% of electrons are kept with a pion rejection factor of about 600. These results are typical across the whole kinematic range.

The results of a pion rejector PID study are shown in Figure 4. Here, the pions (blue) and electrons (red) are selected according to readings in the gas Čerenkov. These distributions are cleanly separated in E/p: a cut at $E/p = 0.54$, corresponding to the magenta line, accepts 99% of electrons while giving a pion rejection factor of about 680.

The combined pion rejection factor from both detectors is expected to be on the order of at least 10^4 pions.

Trigger Efficiency The primary LHRS trigger for E06-014 was the T3 trigger, formed by requiring a hit in both the S1 and S2m scintillator planes; in effect, this requires that one paddle in each scintillator plane record a hit on both its left and its right photomultiplier tubes. The T4 trigger, formed by requiring a hit in two out of three detectors (the S1 scintillator plane, the S2m scintillator plane, and the gas Čerenkov, excluding an S1-S2m coincidence), allows for a check on the T3 efficiency.

In order to determine the T3 trigger efficiency, we start from the equation:

$$\varepsilon_{T3} = \frac{N_{T3}}{N_{T3} + N_{T4}}, \tag{5}$$

where $N_{T3(4)}$ is the number of T3(4)-type events adjusted for prescaling, defined as follows:

$$N_{T3(4)} = ps_{T3(4)} \times \mathrm{bit}_{T3(4)}, \tag{6}$$

where $ps_{T3(4)}$ is the prescale value for the T3(4) trigger and $\mathrm{bit}_{T3(4)}$ is the number of times the bit pattern was set – that is, the number of events that passed the prescale condition. The reason for using this definition for $N_{T3(4)}$ is to avoid a possible situation where some T4 triggers do *not* pass the prescale condition. This would imply (based on Equation 5) that the T3 trigger efficiency is better than it actually is.

Table 1 shows the results binned by LHRS momentum setting. The trigger efficiency proved to be better than 99.9% across the whole kinematic range.

p (GeV)	E (GeV)	ε_{T3} (%)	ε_1 (%)
1.23	1.23	99.992 ± 0.001	98.981 ± 0.192
0.60	4.73	99.949 ± 0.021	99.282 ± 0.592
0.60	5.89	99.959 ± 0.022	99.339 ± 0.430
0.80	4.73	99.934 ± 0.038	99.209 ± 0.843
0.90	5.89	99.948 ± 0.032	99.293 ± 0.796
1.13	5.89	99.928 ± 0.053	99.228 ± 1.037
1.20	5.89	99.978 ± 0.022	99.213 ± 1.307
1.27	5.89	99.937 ± 0.045	99.172 ± 0.967
1.42	4.73	99.952 ± 0.041	99.189 ± 1.235
1.42	5.89	99.926 ± 0.064	98.810 ± 1.176
1.51	4.73	99.919 ± 0.049	99.104 ± 1.149
1.51	5.89	99.962 ± 0.031	99.172 ± 1.326
1.60	4.73	99.959 ± 0.040	98.953 ± 1.421
1.60	5.89	99.956 ± 0.041	98.832 ± 1.413
1.70	5.89	99.956 ± 0.039	98.620 ± 1.924

Table 1: The T3 trigger efficiency ε_{T3} and the VDC one-track efficiency ε_1 for each LHRS kinematic setting.

VDC One-Track Efficiency The inefficiency of the VDCs (Vertical Drift Chambers) is dominated by mistakes in the software computation of tracks, usually as a result of multi-track events or no-track events. In multi-track events, many particles cross the VDC planes simultaneously, resulting in a large number of possible trajectories. Therefore, we retain only one-track events in our analysis of the various physics quantities of interest; however, we need to be aware that such a requirement will discard any good tracks that arrive in multi-track events. To understand the effect of the one-track event requirement, we examine the zero-, multi-, and one-track efficiencies, taking zero- and multi-track efficiencies as the *inefficiency* of the VDC tracking detector [18].

We define the *one-track efficiency* ε_1 as follows: we count the number of one-track events and compare this sum to the sum of all zero-, one-, and multi-track events. Mathematically, we have:

$$\varepsilon_1 = \frac{N_1}{\sum_{i=0}^{4} N_i}, \tag{7}$$

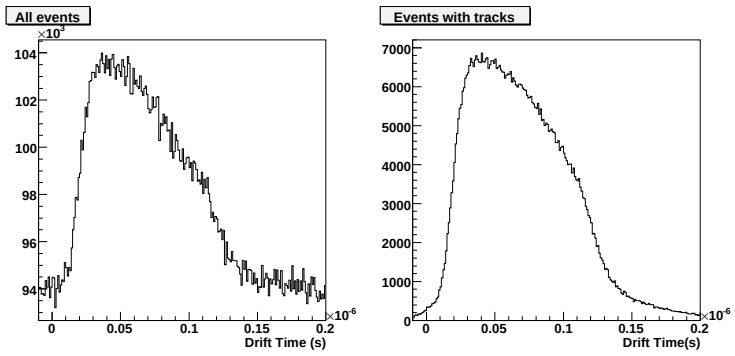

Figure 5: Calibrated t_0 spectrum for second v plane of first MWDC in BigBite, shown for all hits (left) and for hits that are determined by software to be part of tracks.

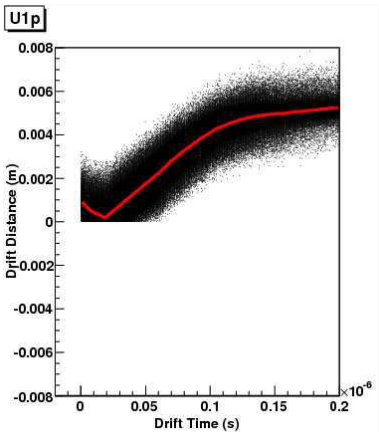

Figure 6: Data (black dots) and parameterization (red line) for time-to-distance conversion in the second u plane of first MWDC in BigBite.

where N_1 is the number of one-track events, and N_i is the number of i-track events ($i = 0, \ldots, 4$). (The software reconstructs a maximum of up to four tracks per event [19, 20].) Similarly, we may determine the other j-track efficiencies ($j \neq 1$) as:

$$\varepsilon_j = \frac{N_j}{\sum_{i=0}^{4} N_i}. \tag{8}$$

We measured one-track efficiencies ε_1 in excess of 99% across our entire kinematic range, as shown in Table 1.

0.1.3 Analysis Progress: BigBite

Data from BigBite will be used to compute the parallel and perpendicular asymmetries $A_\parallel$ and $A_\perp$, which will contribute to our measurement of d_2^n and to our measurement of A_1^n. Since BigBite is not being used to measure a cross section, absolute efficiencies are less important than they are for the Left HRS. Here, we discuss our analysis progress on BigBite data over the past year. In addition to the topics described below, we have begun to study data quality and compute preliminary asymmetries.

Multi-Wire Drift Chambers In order to improve our understanding of the behavior and locations of the wires in the BigBite Multi-Wire Drift Chambers (MWDCs), we have completed a t_0 timing calibration for all planes. This allows us to effectively separate the timing of electrons in the wire chamber from time-of-flight to the shower, and from the timing of the trigger electronics. The results of this calibration are shown in Figure 5; the rising edge of the drift time spectrum shows the t_0 calibration. We then parameterized the relationship between drift time and drift distance (Figure 6) for each plane, which in turn allowed us to calculate the actual wire positions empirically.

Armed with accurate positions for the wires in the MWDCs, we find track residuals for all planes to range from 190 to 265 μm. Figure 7 shows representative residual plots for the six u planes.

Optics We took as a starting point the BigBite optics package for E06-010 [21], which allowed us to rapidly achieve an excellent vertex reconstruction (Figure 8) with centimeter-level resolution.

For our momentum reconstruction, we deviated from the E06-010 approach. We adapted its first-order optics model, which places the proton peak from our 1.232-GeV, elastic H_2 calibration data at $W = 0.938$ GeV/c^2. For particles with very low momenta, at the edge of the BigBite acceptance, a further correction factor is then necessary in order to place the Δ peak at $W = 1.232$ GeV/c^2; we therefore applied the E06-010

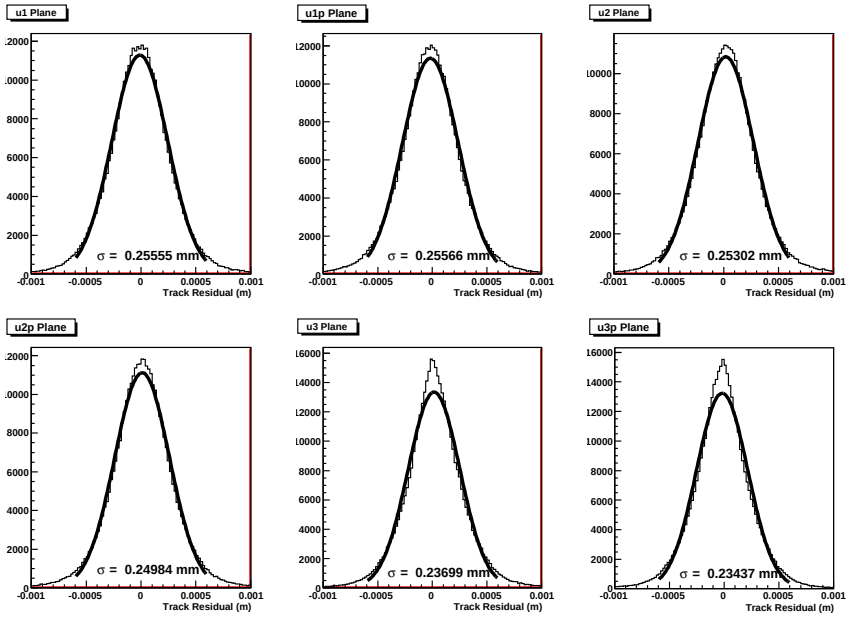

Figure 7: Track residuals for u planes in the multi-wire drift chambers.

optics package's linear correction at low momenta. This correction, however, is not continuous in the first derivative with the uncorrected momentum, resulting in a sharp discontinuity in the momentum spectrum at 0.9 GeV/c (Figure 9). To restore continuity to our momentum reconstruction, we derived a quadratic function that smoothes the transition between the low-momentum region and the rest of the spectrum. With $p^{(1)}$ the first-order momentum, the final reconstructed momentum p is then of the form

$$p = \begin{cases} p^{(1)} & \text{for } p^{(1)} > 0.95 \text{ GeV} \\ p^{(1)} - 3.7\left(p^{(1)} - 0.95 \text{ GeV}\right)^2 & \text{for } 0.85 \leq p^{(1)} \leq 0.95 \text{ GeV} \\ p^{(1)} + 0.148\left(p^{(1)} - 0.9 \text{ GeV}\right) & \text{for } p^{(1)} < 0.9 \text{ GeV} \end{cases} \tag{9}$$

Figure 10 shows the resulting invariant mass spectrum for elastic scattering from hydrogen atoms. Figure 11 shows a momentum resolution of 1.1% for the same data.

Shower and Preshower The preshower and shower detectors in BigBite are arrays of lead-glass blocks designed to capture the energy of an incident particle. The 54 preshower blocks are arranged in a 2×27 array, and the 189 shower blocks form a 7×27 array. Each block is mated to a photomultiplier tube (PMT). The signals from a cluster of adjacent blocks are summed to determine the energy of the particle that produced the signal.

The energy E_i deposited in the i^{th} shower or preshower block is related to the signal amplitude A_i and pedestal P_i according to

$$E_i = C_i \left(A_i - P_i\right) \tag{10}$$

The coefficients C_i must be determined via calibration of the total shower and preshower signal to the corresponding track momentum, reconstructed using the BigBite optics. We compute the 243 total coefficients using a linear fit to minimize χ^2, the square of the difference between the reconstructed momentum p and the total energy reported by both the preshower and the shower. Over M good electron tracks, χ^2 is given by

$$\chi^2 = \sum_{i=1}^{M} \left[p_i - \sum_{j=1}^{N^{ps}} C_{ij}^{ps} \left(A_{ij}^{ps} - P_j^{ps}\right) - \sum_{k=1}^{N^{sh}} C_{ik}^{sh} \left(A_{ik}^{sh} - P_k^{sh}\right) \right]^2 \tag{11}$$

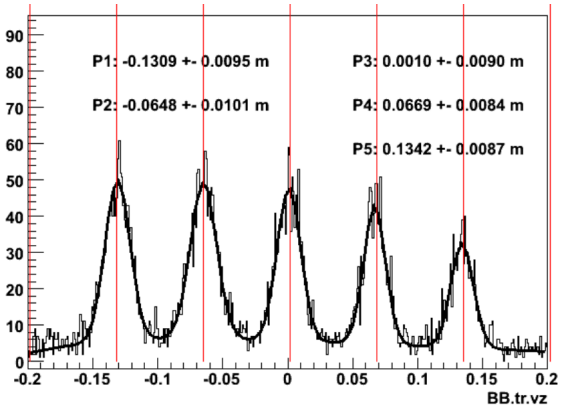

Figure 8: Vertex reconstruction for tracks belonging to negatively-charged particles issuing from a carbon-foil target in a five-pass run. The measured peak locations are compared to the surveyed foil positions, marked in red.

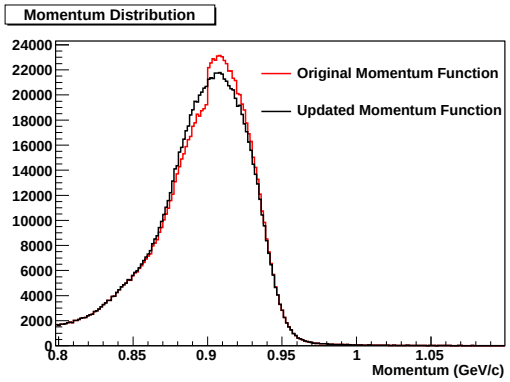

Figure 9: Momentum spectrum for negatively charged particles in data taken with a beam energy of 1.232 GeV and an H_2 target. The red histogram shows the momentum spectrum resulting from the linear low-momentum correction in the E06-010 optics package. The black histogram makes use of the correction described by Equation 9.

where N^{ps} and N^{sh} are the number of blocks in a preshower cluster and in a shower cluster, respectively [22].

We have completed a shower and preshower calibration using several four-pass production runs, taken relatively late in the E06-014 experiment. Figure 12 shows E plotted against p; the densely populated region along $E \approx p$ corresponds to the expected value for electrons.

E06-014 ran for six weeks, during which radiation damage slowly yellowed the lead-glass preshower and shower blocks. Consequently, the quality of this calibration must be checked over a wide time range, and the run period will likely be divided into successive time windows, each with its own energy calibration.

Gas Čerenkov E06-014 was the commissioning experiment for the BigBite gas Čerenkov, which was placed in the detector stack between the multi-wire drift chambers and the preshower. Its purpose was to aid in removing pion contamination, both in the online trigger and in offline analysis. We have completed an LED calibration and preliminary pion rejection and electron efficiency calculations, treating the two sides (beam side and RHRS side) separately due to the fact that their rates differed by an order of magnitude.

The twenty PMTs of the gas Čerenkov, each with coverage of a slightly different region of the detector, are calibrated using LED runs. Figure 13 shows a representative ADC spectrum from such a run. We used a convolution of Gaussian and Poisson functions to fit the pedestal and the single-photoelectron peak, allowing us to adjust our settings to place the single-photoelectron peak at thirty ADC channels above the pedestal.

Figures 14 and 15 show the ADC signal spectra in the gas Čerenkov for accidentals (in blue) and for particles coincident with the trigger (in red), for both high-rate (beam side) and low-rate (RHRS side) parts of the detector. Here, accidentals are defined as events where the Čerenkov TDC timing fell outside the T2 trigger timing window; particles coincident with the trigger have timing within that window.

To compute preliminary pion rejection factors and electron efficiencies, we applied cuts on preshower energy and E/p in order to select a pion sample (Figure 16) and an electron sample (Figure 17). The E/p value for each event comes from the total energy (shower and preshower) and the reconstructed momentum for the track.

Our first task is to determine how efficiently we can reject pions using a cut on the ADC signal corresponding to the particular PMT that should have detected the pion track. We define the pion rejection factor ϵ_π as

$$\epsilon_\pi = \frac{N_\pi^{total}}{N_\pi^{accept}} \tag{12}$$

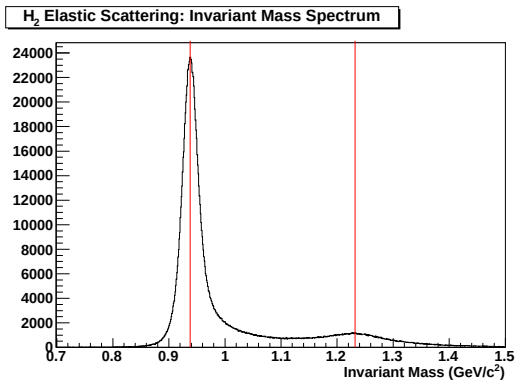

Figure 10: Reconstructed invariant mass spectrum for H_2 elastics data in BigBite. The red lines mark the known masses of the proton and of the $\Delta(1232)$.

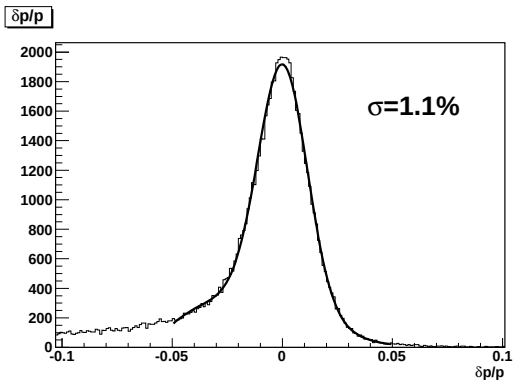

Figure 11: Momentum resolution for BigBite negative optics, plotted as $\delta p/p = (p - p_{elas})/p$.

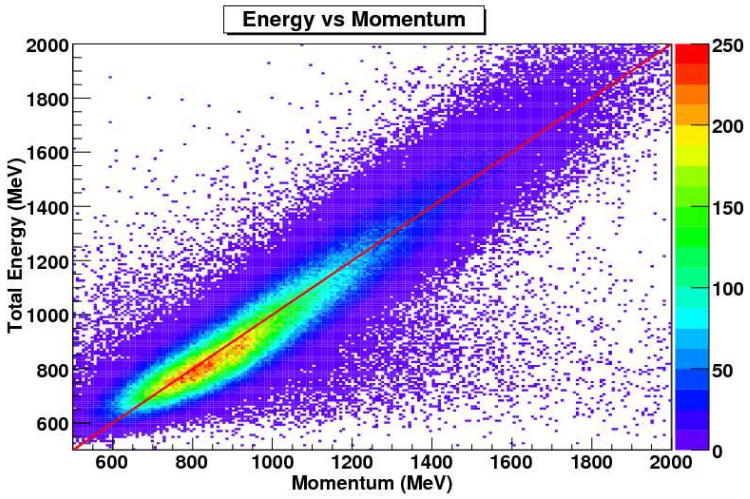

Figure 12: Distribution of E vs p for calibrated preshower and shower. The red line at 45° highlights the ideal condition in which the reconstructed momentum and energy are equal.

where N_π^{total} is the total number of events in the pion sample (as selected from shower and preshower data) and N_π^{accept} is the number of those events that pass the Čerenkov ADC cuts and are thus misidentified as electrons. We calculated ϵ_π independently for several choices of cut threshold; the preliminary results, averaged over each side of the detector, are shown in Figure 18. At best, we see a pion rejection factor of about 200 on the small-angle side, while the large-angle side sees a pion rejection factor closer to 900; we believe this discrepancy is due to hardware issues associated with the rate difference between the two sides.

We have also made preliminary determinations of the detector's electron efficiency – that is, the degree to which electrons pass the Čerenkov ADC cuts rather than being misidentified as pions. We began with an electron sample determined by shower and preshower data (Figure 17). Where N_e^{total} is the number of events in this electron sample, we define the electron efficiency ϵ_e as

$$\epsilon_e = \frac{N_e^{accept}}{N_e^{total}} \tag{13}$$

where N_e^{accept} is the number of events in the electron sample that pass the ADC cuts. We computed ϵ_e in three ways for each PMT. First, we calculated the efficiency for a zero-photoelectron ADC cut, i.e. the

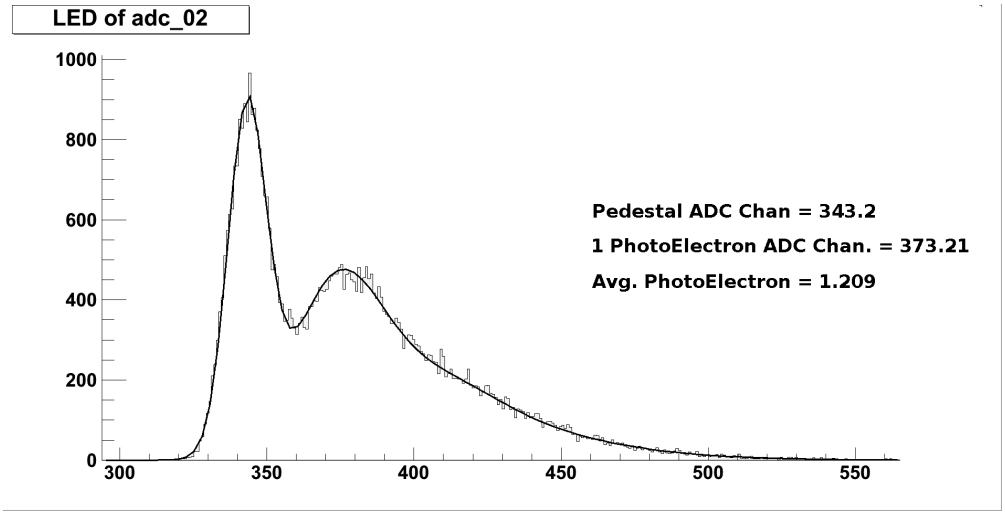

Figure 13: Calibrated spectrum of a BigBite gas Čerenkov PMT for an LED run. Fits to the pedestal and single-photoelectron peak allowed the latter to be aligned at the 30-channel mark.

detection efficiency. Second, we repeated the calculation for a three-photoelectron ADC cut. Finally, in order to account for the statistical fact that real electrons will not always produce three or more photoelectrons even under ideal circumstances, we fit a Poisson distribution to the ADC spectrum of each PMT. This allowed us to compute the expected electron efficiency for a three-photoelectron cut.

Figure 19 shows preliminary ϵ_e values for the small-angle side of the detector; preliminary results for the large-angle side are shown in Figure 20. With the exception of PMTs 1 and 8, which are on the upper and lower edges of the acceptance, we measured a detection efficiency greater than 90% in all PMTs. The expected efficiencies for a three-photoelectron cut are generally consistent with the detection efficiencies, but the efficiencies for the empirical three-photoelectron cut drop as low as 50% for PMTs at the top and bottom of the acceptance on the high-rate, small-angle side. In general, as with pion rejection, we measured significantly better performance on the large-angle side, where rates were lower; here, even empirical three-photoelectron cuts routinely resulted in better than 90% electron efficiencies.

0.1.4 Analysis Progress: Target

E06-014 used the standard Hall A polarized ^{3}He target with two holding field directions: longitudinal and transverse in-plane with respect to the beam direction. To extract the target polarization, we have conducted several measurements to calibrate different target system components.

Target Density Knowledge of the ^{3}He target density is crucial for the extraction of the target polarization and the cross sections. The target's cell density is measured by observing the collisional absorption broadening of the D1 and D2 resonance lines of the alkali metal rubidium (Rb) in the presence of the ^{3}He gas [23]. We have measured and fit the absorption spectra to compute an ^{3}He density, including its pressure broadening (PB), of 8.099 $\pm$ 0.032 amg, where an amagat (amg) is 2.687 $\times 10^{25}$ m^{-3}.[1]

Thickness of Target Cell The cell's glass entrance window and side wall thicknesses are essential input parameters in the calculation of radiative corrections and in the extraction of cross sections. The determination of a transparent thin-film thickness can be performed by taking advantage of the interference of the reflected light from the front surface of the film and the reflected/refracted light from its back internal surface, as is shown in Figure 21. This interference depends on the difference of the two optical path lengths, and hence on the relative phase of the interacting waves [24].

[1]For reference, a comparable measurement of the ^{3}He density in this cell was performed at the University of Virginia before the experiment. The result, including PB, was 7.99 $\pm$ 0.01 amg.

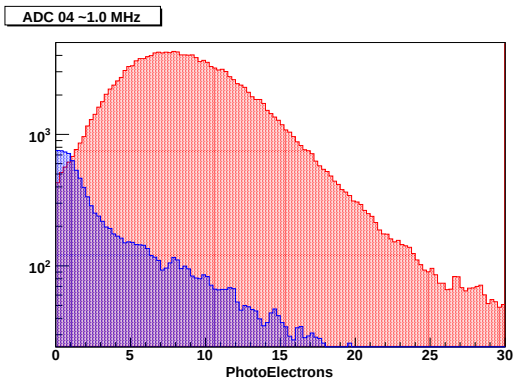

Figure 14: BigBite gas Čerenkov ADC signal spectra for a beam-side PMT with a rate of about 1 MHz. Particles in the blue histogram are accidentals while particles in the red histogram could have caused the trigger, as determined by their TDC timing relative to the trigger window.

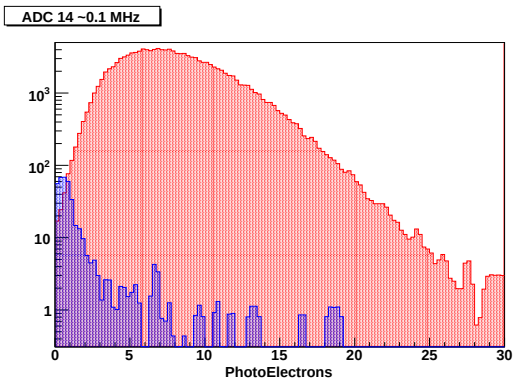

Figure 15: BigBite gas Čerenkov ADC signal spectra for a RHRS-side PMT with a rate of about 0.1 MHz. Particles in the blue histogram are accidentals while particles in the red histogram could have caused the trigger, as determined by their TDC timing relative to the trigger window.

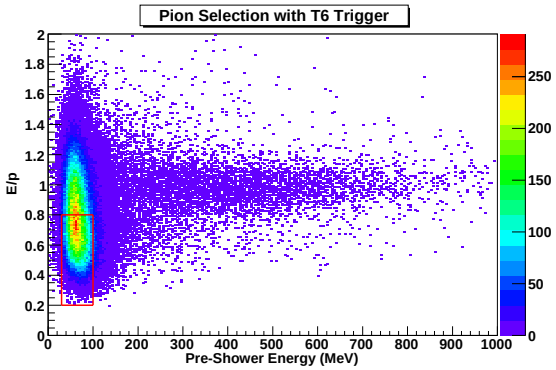

Figure 16: Pion selection for BigBite gas Čerenkov studies.

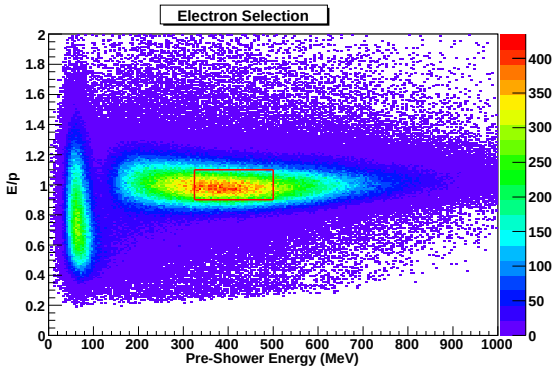

Figure 17: Electron selection for BigBite gas Čerenkov studies.

We have performed several data scans to measure the glass thickness of the polarized ^{3}He and reference cells, called Samantha and GMA respectively. Tables 2 and 3 summarize the side wall and window thicknesses of the two cells. The statistical uncertainty of each measurement is about 2%. The main systematic uncertainty (of $< 1\%$) comes from the determination of the tilt angle between the incident laser and the glass.

Electron Paramagnetic Resonance A measurement of an electron paramagnetic resonance (EPR) uses the stimulated light emission from the target's alkali metals as a magnetometer. This allows us to measure the net change in the magnetic field magnitude seen by the Rb atoms in the pumping chamber when the ^{3}He nuclei are polarized in alignment with the external holding field, compared to when their spins are anti-aligned with the same holding field. A summary of the EPR polarization extracted from the measurements taken during the E06-014 running period is shown in Figure 22. Figure 23 shows preliminary polarization measurements for the whole E06-014 running period, based on roughly calibrated NMR measurements and an interpolation of the pumping chamber polarization from the EPR measurements.

Nuclear Magnetic Resonance A water calibration study is in progress and will allow us to determine the target's polarization using the adiabatic fast passage (AFP) nuclear magnetic resonance (NMR) mea-

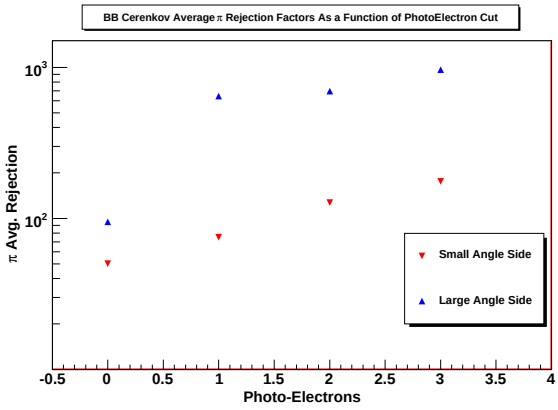

Figure 18: Average pion rejection factors for the BigBite gas Čerenkov, plotted as a function of the threshold of the Čerenkov ADC cuts. Small- and large-angle averages are plotted separately due to the rate difference between the sides. PMTs 9, 10, 19 and 20 (at the bottom of the detector stack) were not included in the calculation because they are outside our acceptance.

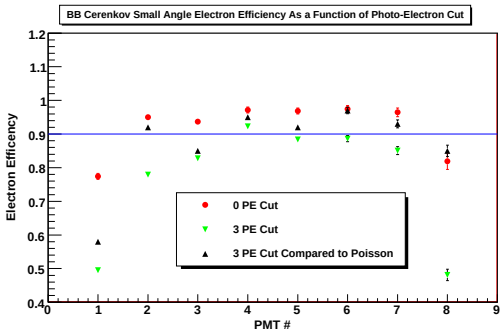

Figure 19: BigBite gas Čerenkov electron efficiency (small-angle side). We have drawn a line at 90% to guide the eye. PMTs 9 and 10 are outside our acceptance.

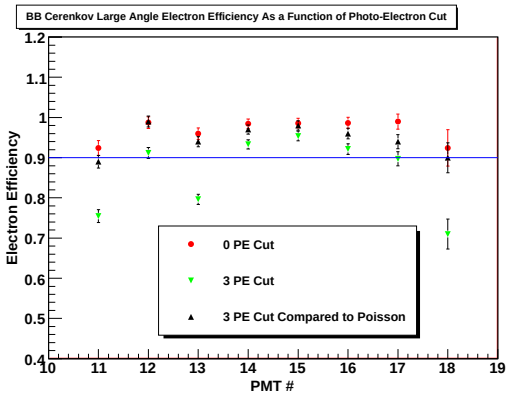

Figure 20: BigBite gas Čerenkov electron efficiency (large-angle side). We have drawn a line at 90% to guide the eye. PMTs 19 and 20 are outside our acceptance.

surements taken during the experiment. Since these measurements were performed only three times a day, we will need to interpolate the results in time in order to arrive at a target polarization for each production run. The final target chamber polarization number for each run will be an average of the interpolated NMR result with the interpolated EPR result.

References

[1] M. Burkardt, hep-ph/0905.4079v1 (2009).

[2] E. Stein *et al.*, Phys. Lett. B **343**, 369 (1995).

[3] M. Burkardt, AIP Conference Proceedings **1149**, 62 (2008), hep-ph/0902.0163v1.

[4] S. Choi, Z.-E. Meziani, X Jiang, B. Sawatzky, *et al.*, Jefferson Lab PAC PR-06-014 (2005).

[5] T. Averett, W. Korsch, Z.-E. Meziani, B. Sawatzky*et al.*, Jefferson Lab PAC E1206121 (2010).

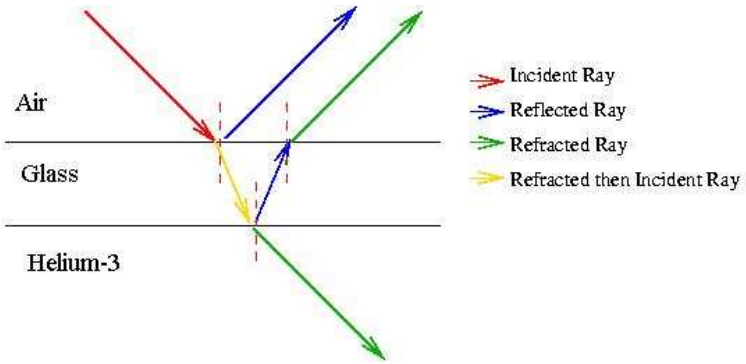

Figure 21: Illustration of the interference phenomenon.

Point	Position (cm)	Glass Thickness (mm)
A	2.5→W1	1.81
B	12.5→W1	1.69
C	20.3→W1	1.74
D	23.4→W1	1.75
E	36.4→W1	1.73
F	3.0→W2	1.72
G	9.0→W2	1.68
H	20.0→W2	1.64
I	28.4→W2	1.66
J	37.4→W2	1.70
W1	-	0.13
W2	-	0.13

Table 2: Fit results for the thickness of the reference cell (GMA). The positions of each measurement point are given with respect to W1 and W2, the upstream and downstream cell windows. Points A-E are on the beam right side of the target and points F-J are on beam left.

[6] X. Zheng *et al.*, Phys. Rev. Lett. **92**, 012004 (2004).

[7] X. Zheng *et al.*, Phys. Rev. C **70**, 065207 (2004).

[8] K. V. Dharmawardane *et al.*, Phys. Lett. B **641**, 11 (2006).

[9] G. Cates, N. Liyanage, Z.-E. Meziani, G. Rosner, B. Wojtsekhowski, X. Zheng, *et al.*, Jefferson Lab PAC E1206122 (2006).

[10] G. Cates, J.-P. Chen, Z.-E. Meziani, X. Zheng *et al.*, Jefferson Lab PAC E1210101 (2010).

[11] H. Avakian, S.J. Brodsky, A. Deur, and F. Yuan, Phys. Rev. Lett. **99**, 082001 (2007).

[12] E. Leader, A. V. Sidorov, and D. B. Stamenov, Int. J. Mod. Phys. **A13**, 5573 (1998).

[13] D. Adams *et al.*, Phys. Lett. B **357**, 248 (1995).

[14] P. L. Anthony *et al.*, Phys. Rev. D **54**, 6620 (1996).

[15] K. Ackerstaff *et al.*, Phys. Lett. B **404**, 383 (1997).

[16] K. Abe *et al.*, Phys. Rev. Lett. **79**, 26 (1997).

[17] K. Abe *et al.*, Phys. Rev. D **58**, 112003 (1998).

Point	Position (cm)	Glass Thickness (mm)
A	2.5→W1	1.56
B	12.5→W1	1.56
C	20.3→W1	1.75
D	25.4→W1	1.70
E	35.6→W1	1.70
F	2.5→W2	1.70
G	11.4→W2	1.67
H	19.1→W2	1.67
I	26.7→W2	1.61
J	35.6→W2	1.68
W1	-	0.12
W2	-	0.13

Table 3: Fit results for the thickness of the polarized ^{3}He cell (Samantha). The positions of each measurement point are given with respect to W1 and W2, the upstream and downstream cell windows. Points A-E are on the beam right side of the target and points F-J are on beam left.

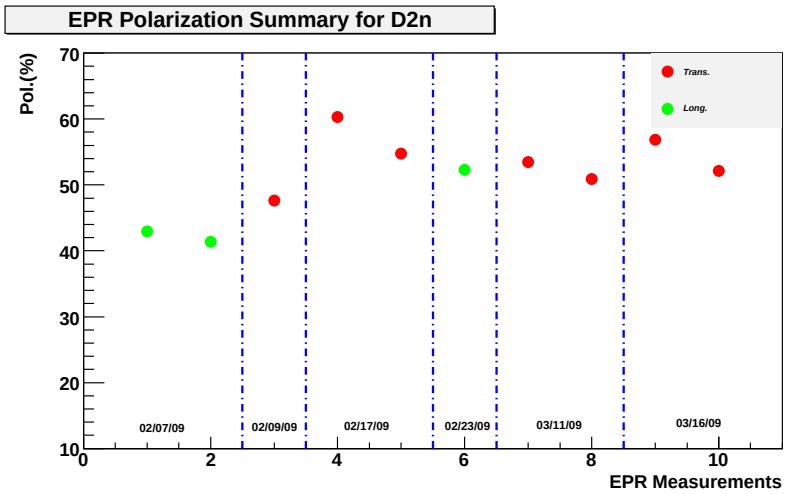

Figure 22: EPR measurements.

[18] P. H. Solvignon, PhD thesis, Temple University (2006).

[19] J. Alcorn *et al.*, Nucl. Instr. and Meth. in Phys. Res. A **522**, 294 (2004).

[20] A. Orsborn. *Report for DoE Science Undergraduate Laboratory Internship Program* (2005).

[21] X. Qian, PhD thesis, Duke University (2010).

[22] K. Allada, PhD thesis, University of Kentucky (2010).

[23] I. Kominis, PhD thesis, Princeton University (2001).

[24] E. Hecht. *Optics*, Addison-Wesley (2002).

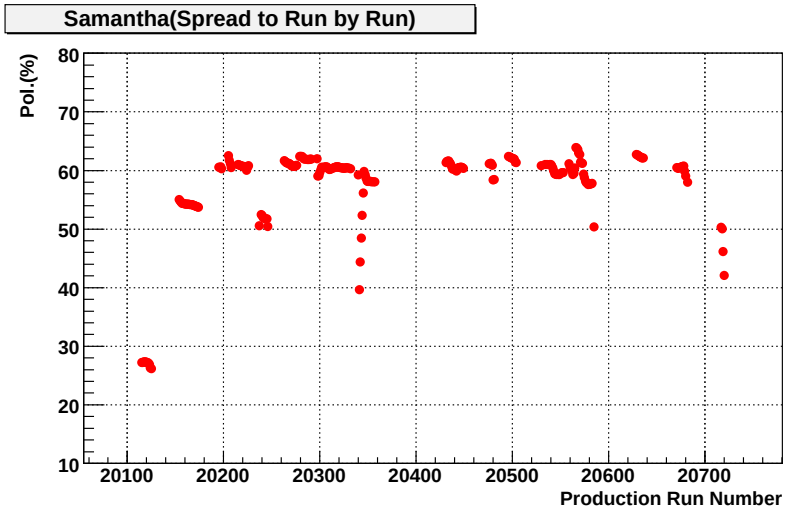

Figure 23: Preliminary pumping chamber polarization calibrated by the EPR measurements.